RSC Advances

PAPER

View Article Online
View Journal | View Issue

Cite this: *RSC Adv.*, 2026, **16**, 10479

Hydrothermal synthesis of nitrogen- and sulfur-co-doped carbon quantum dots from rice straw for fluorescent detection of Hg^{2+} in aqueous media

Duc Cuong Nguyen, [a] Bao Long Hoang, [a] Van Duong Pham, [b] Hop Bao Tung Nguyen, [a] Tuan Anh Pham [a] and Thi Thao Vu *[a]

Received 17th December 2025
Accepted 12th February 2026

DOI: 10.1039/d5ra09779g

rsc.li/rsc-advances

Biomass-derived carbon quantum dots (CQDs) have emerged as promising fluorescent nanomaterials owing to their low toxicity, cost-effectiveness, and facile synthesis, making them attractive for sensing applications. In this study, nitrogen- and sulfur-co-doped CQDs (NS-CQDs) were synthesized from rice straw *via* a simple and low-cost hydrothermal route using gelatin and dimethyl sulfoxide as nitrogen and sulfur sources, without the need for strong acids or advanced processing techniques. The as-prepared NS-CQDs exhibited intense blue emission with a high quantum yield of 39.7%, significantly exceeding that of undoped CQDs. A fluorescence-based sensing platform was constructed using the NS-CQDs, which showed high selectivity and sensitivity toward Hg^{2+} ions, with a wide linear detection range of 0–100 μM and a low detection limit of 0.148 μM, enabling practical mercury monitoring. Spectroscopic and electrokinetic analyses indicate that fluorescence quenching is governed predominantly by static complex formation between Hg^{2+} and surface O-, N-, and S-containing functional groups, with a minor contribution from dynamic quenching. Furthermore, application to real water samples demonstrated reliable recoveries and good reproducibility. This work provides a sustainable strategy for valorizing agricultural residues into high-performance fluorescent nanomaterials and offers a promising platform for environmental mercury monitoring.

1 Introduction

The rapid advancement of science and technology, coupled with the intensified exploitation of natural resources to support economic and industrial growth, has resulted in substantial progress in manufacturing, mining, and infrastructure development. However, these activities have also led to the widespread release of toxic heavy metal ions from industrial effluents and ore-processing operations involving rare earths, iron, and copper. Such emissions contribute significantly to the contamination of aquatic environments, posing severe risks to ecosystems and human health.[1,2] Among these contaminants, mercury (Hg^{2+}) is particularly hazardous owing to its high toxicity, persistence, and bioaccumulation potential. It exhibits a strong affinity for thiol groups in proteins and enzymes, resulting in irreversible damage to the brain, kidneys, and central nervous system.[3–5] Consequently, the development of rapid, cost-effective, and reliable detection methods for mercury and other heavy metals in environmental water sources has become an urgent global priority.[6]

To date, several conventional analytical techniques have been employed for mercury detection, such as inductively coupled plasma mass spectrometry (ICP-MS),[7] atomic fluorescence spectroscopy (AFS),[8] and electrochemical approaches.[9] While these techniques offer excellent sensitivity and precision, their practical application is often constrained by the requirement for expensive instrumentation, labor-intensive sample preparation, and skilled operation. To overcome these limitations, fluorescence-based nanosensors have emerged as promising alternatives for heavy-metal detection due to their high sensitivity, rapid response, and ease of implementation. Among them, carbon quantum dots (CQDs) have gained particular attention owing to their excellent water solubility, low cytotoxicity, photostability, and facile synthesis.[10,11]

The optical and sensing properties of carbon quantum dots (CQDs) can be effectively tuned through heteroatom doping (*e.g.*, N, S, or P), which modifies their electronic band structure, surface states, and chemical reactivity.[12,13] The comparable atomic radii and electronegativities between carbon and dopant atoms contribute to enhanced fluorescence emission and improved metal-ion binding affinity.[14] Consequently, heteroatom-doped CQDs have been widely investigated as fluorescent probes for the selective detection of Hg^{2+} ions.[15,16]

[a]*Faculty of Engineering Physics and Nanotechnology, VNU University of Engineering and Technology (VNU-UET), 144 Xuan Thuy Street, Cau Giay, Hanoi 100000, Vietnam. E-mail: vtthao@vnu.edu.vn*

[b]*Institute of Physics, Vietnam Academy of Science and Technology, 10 Dao Tan Street, Giang Vo, Hanoi 100000, Vietnam*

For example, Liu *et al.* synthesized nitrogen- and sulfur-co-doped CQDs (NS-CQDs) using cysteine and polyethyleneimine as precursors, achieving high selectivity and sensitivity for Hg^{2+} detection in real samples.[17] Similarly, Wu and Tong prepared NS-CQDs *via* a hydrothermal process employing ammonium citrate and L-cysteine, demonstrating excellent analytical performance toward mercury ions.[18]

More recently, increasing attention has been devoted to biomass-derived carbon nanomaterials as sustainable fluorescent probes for heavy-metal detection. Carbon materials prepared from diverse agricultural and waste biomass sources have demonstrated high sensitivity toward toxic metal ions such as Hg^{2+}, Pb^{2+}, and Cu^{2+}.[19–24] For example, Jaswal *et al.* utilized banana stem biomass to prepare activated carbon as a fluorescent probe for the sensitive detection of mercury in wastewater, highlighting the valorization of low-cost agricultural residues for environmental sensing applications.[19] Liang *et al.* developed biomass-derived carbon dots from plant-based feedstock and incorporated them into a carboxymethyl cellulose hydrogel matrix for the selective detection and visual adsorption of Cu^{2+} ions.[20] Sharma and Singh reported waste biomass–derived nano-carbon engineered *via* catalytic treatment for the ultra-trace detection of both Pb^{2+} and Hg^{2+}, demonstrating the effectiveness of surface-modified biomass carbon for dual-metal sensing.[21] Khare *et al.* synthesized carbon quantum dots from *Triticum aestivum* (wheat) biomass using a deep eutectic solvent route, achieving nanomolar-level fluorescence sensing of Hg^{2+} and glutathione.[22] Bavya *et al.* prepared carbon dots from bamboo cellulose and designed a fluorescence-enhanced sensor for mercury detection, underscoring the role of biomass-derived polysaccharides in tuning optical responses.[23] In addition, Pan *et al.* reported a DMF-mediated synthesis of N,S-co-doped carbon quantum dots from biomass precursors, in which fluorescence quenching toward Hg^{2+} was governed by surface complexation mechanisms.[24] However, achieving high selectivity for Hg^{2+} in complex aqueous environments remains challenging due to potential interference from other toxic heavy metal ions commonly present in environmental matrices.

Despite these advances, most reported biomass-derived CQDs for metal-ion sensing rely on a limited range of precursor types or focus primarily on undoped systems, and systematic studies integrating renewable agricultural waste with controlled heteroatom co-doping and detailed sensing mechanism analysis remain scarce. In particular, the development of rice straw-derived CQDs with tailored nitrogen and sulfur functionalities for selective Hg^{2+} detection has been insufficiently explored.

In this work, nitrogen- and sulfur-co-doped carbon quantum dots (NS-CQDs) were synthesized *via* a simple hydrothermal route using rice straw as a renewable and low-cost carbon precursor. Rice straw is one of the most abundant agricultural residues worldwide, generated in large quantities during rice production, and is often disposed of through open-field burning, which contributes significantly to air pollution and greenhouse gas emissions.[25,26] The valorization of rice straw as a carbon source therefore offers both environmental and economic advantages by mitigating waste-related pollution while enabling the production of value-added nanomaterials. Gelatin and dimethyl sulfoxide were employed as independent nitrogen and sulfur dopant sources, respectively, enabling controlled co-doping to tailor the surface chemistry and optical properties of the CQDs. The fluorescence response of the resulting NS-CQDs toward Hg^{2+} ions was systematically investigated, including selectivity and interference effects in aqueous media. Furthermore, spectroscopic techniques were used to examine the interaction between mercury ions and surface functional groups on the NS-CQDs. The applicability of the proposed nanosensor was evaluated using real water samples, highlighting the potential of biomass-derived CQDs as sustainable fluorescent probes for environmental monitoring.

2 Experimental section

2.1 Materials

The carbon precursor, rice straw, was sourced from agricultural cooperatives in Ninh Binh Province, Vietnam. The collected straw was thoroughly washed with deionized water followed by distilled water to remove impurities, dried at 70 °C for 3 days, and subsequently cut into fibers of approximately 1 mm in length. Gelatin, dimethyl sulfoxide (DMSO, 99.5%), and citric acid ($C_6H_8O_7$, 99.5%) were purchased from Xilong (China). The metal salts NaCl (98%), KCl (99%), $CuCl_2$ (99.7%), $Zn(NO_3)_2$ (98%), $CaCl_2$ (96%), $FeCl_3$ (99%), $AgNO_3$ (99%), $MgSO_4$ (99%), $HgNO_3$ (99.5%), $MnCl_2$ (99%), $NiCl_2$ (98%), $Ba(NO_3)_2$ (98%), $CoCl_2$ (98%), glacial acetic acid (99.5%), HCl (36%), NaOH (97%), and CH_3COONa (98%) were purchased from Xilong (China). The metal salts $PdCl_2$ (99.99%), $CdCl_2$ (98%), and $PbCl_2$ (98%) were purchased from Sigma-Aldrich (USA). All reagents were of analytical grade, and Millipore water was used in all experiments.

2.2 The synthesis of NS-CQDs

After being purchased, the rice straw was thoroughly washed several times with distilled water to remove impurities. The washed material was then dried and ground into a fine powder. The rice straw powder was carbonized under a nitrogen atmosphere at 600 °C for 2 hours. One gram of the resulting carbon was mixed with distilled water and DMSO, followed by continuous stirring at 1000 rpm for 30 minutes. Citric acid and gelatin, in a 1 : 2 ratio, were then added to the initial carbon mixture, and stirring was continued until a homogeneous solution was obtained. The mixture was transferred into a Teflon-lined autoclave and heated at 200 °C for 8 hours. Upon completion of the reaction, the autoclave was allowed to cool naturally to room temperature. After being cooled, the large and heavy residues that settled at the bottom were removed by centrifugation. The supernatant was collected and further purified through multiple filtration and chromatographic steps to obtain the highest possible purity. For long-term storage, the solution was dried to yield CQDs in the form of a brown powder. When dissolved in distilled water, the CQD solution exhibited

Fig. 1 Synthesis process of nitrogen- and sulfur-co-doped carbon quantum dots (NS-CQDs) from rice straw.

blue photoluminescence under UV light excitation. Fig. 1 illustrates the synthesis process of NS-CQDs.

2.3 Detection of Hg^{2+} with NS-CQDs

A mixture was prepared by combining 750 μL of acetate buffer solution (NaAc–HAc, 0.2 M, pH 5.0), 100 μL of the NS-CQD solution, and varying concentrations of Hg^{2+} ions, followed by dilution with deionized water to a final volume of 3 mL. After incubation at room temperature for approximately 2 min, the fluorescence intensity of the NS-CQDs was measured using a fluorescence spectrometer.

2.4 Real sample assays

Aqueous media were collected from the laboratory, and a water sample was obtained from the To Lich River in Hanoi, Vietnam. Both samples were subsequently filtered through a membrane filter to remove suspended particulates. An aliquot of 200 μL of either aqueous media or To Lich River water was mixed with varying concentrations of Hg^{2+}, acetate buffer solution (NaAc–HAc, 0.2 M, pH 5.0), and then supplemented with 100 μL of NS-CQDs. The resulting mixture was diluted with deionized water to a final volume of 3 mL. Following incubation at room temperature for approximately 2 min, the fluorescence intensity of the NS-CQDs was measured using a fluorescence spectrophotometer.

2.5 Characterization

The optical and structural properties of the synthesized NS-CQDs were comprehensively characterized using a combination of spectroscopic and microscopic techniques, while the thermal decomposition behavior of rice straw was analyzed using thermogravimetric (TGA-DTG) analysis.

TGA-DTG was performed using a macro-thermogravimetric system (Macro-TGA) to evaluate the thermal stability and compositional characteristics of rice straw. The measurements were carried out under a nitrogen atmosphere within the temperature range of 36–962 °C at a controlled heating rate of 10 °C min^{-1}. This analysis provided detailed insights into the multistage decomposition behavior of the rice straw precursor, including the relative contributions of hemicellulose, cellulose, and lignin components, as well as the overall thermal degradation profile of the biomass.

UV-Vis absorption spectroscopy was employed to examine the electronic transitions and optical behavior of the CQDs within the wavelength range of 250–700 nm. Measurements were conducted using a Hitachi UH5300 spectrophotometer with a 10 mm quartz cuvette.

Photoluminescence (PL) spectroscopy was utilized to investigate the emission characteristics of the CQDs. Upon excitation with light of sufficient energy, electrons were promoted to higher energy levels and subsequently relaxed, emitting fluorescence photons. The PL spectra were recorded over the range of 310–700 nm using an FLS1000 Photoluminescence Spectrometer (Edinburgh Instruments, UK). For pH-dependent PL measurements, the CQD dispersion (0.1 mg mL^{-1}) was divided into aliquots with pH adjusted between 1 and 14 using 0.1 M HCl or 0.1 M NaOH. Each sample was sonicated for 5 min and equilibrated for 30 min before measurement. The PL spectra were recorded under identical conditions using an excitation wavelength of 340 nm. Time-resolved photoluminescence (TRPL) spectra were acquired using an FLS1000 Photoluminescence Spectrometer (Edinburgh Instruments, UK), equipped with a pulsed LED light source operating at a power of 40 μW per pulse. The excitation and emission wavelengths were 375 nm and 430 nm, respectively.

The fluorescence quantum yield (QY) of the CQDs was determined using quinine sulfate in 0.1 M H_2SO_4 as a reference standard ($\phi_{st} = 54\%$) at 350 nm excitation).[27] To minimize self-absorption effects, the absorbance of both the sample and standard was kept below 0.1. The relative quantum yield (ϕ_x) was calculated according to the equation:[27,28]

$$\phi_x = \phi_{st}\left(\frac{I_x}{I_{st}}\right)\left(\frac{A_{st}}{A_x}\right)\left(\frac{\eta_x}{\eta_{st}}\right)^2, \quad (1)$$

where I, A, and η represent the integrated emission intensity, absorbance, and solvent refractive index, respectively, and the subscripts "st" and "x" refer to the standard and sample. Since the solvents used had similar refractive indices, $\frac{\eta_x}{\eta_{st}} \approx 1$.

Fourier Transform Infrared (FT-IR) spectroscopy was carried out using a Nicolet™ iS50 spectrometer in the range of 4000–400 cm^{-1} to identify the surface functional groups of the CQDs.

X-ray photoelectron spectroscopy (XPS) was used to analyze the surface elemental composition and chemical bonding states of the synthesized NS-CQDs. The measurements were performed on an ULVAC-PHI Genesis 500 spectrometer equipped with a monochromatic Al Kα radiation source ($h\nu = 1486.6$ eV). To ensure data reliability, XPS spectra were collected at three different spots on each sample, and the reported atomic percentages represent the average values with corresponding standard deviations. Survey spectra were acquired to determine the elemental composition, followed by high-resolution scans of the C 1s, N 1s, O 1s, and S 2p regions for detailed chemical-state analysis. All binding energies were calibrated using the C 1s peak at 284.9 eV as a reference. Peak deconvolution was conducted using multi-Gaussian fitting.

Energy-dispersive X-ray spectroscopy (EDX) was employed to analyze the elemental composition and spatial distribution of the synthesized NS-CQDs. EDX measurements were carried out using an EDX detector coupled to a field-emission scanning electron microscope (FE-SEM, JEOL JSM-IT800). Prior to analysis, the NS-CQDs were drop-cast onto a clean silicon substrate and dried under ambient conditions. Elemental mapping was performed over selected regions to visualize the distribution of C, O, N, S, and other detectable elements. The acquired spectra and elemental maps were processed using the instrument's built-in analysis software.

Transmission Electron Microscopy (TEM) images were acquired with a JEOL JEM-2100 electron microscope to examine the morphology, size, and crystallinity of the NS-CQDs.

Finally, zeta potential and electrophoretic mobility measurements were carried out using a HORIBA SZ-100-Z2 analyzer at 25.1 °C, with applied electrode voltages of 2.7 V for the NS-CQDs sample and 1.2 V for the NS-CQDs–Hg^{2+} complex.

3 Results and discussion

3.1 TGA-DTG analysis of rice straw

The thermal decomposition behavior of rice straw was examined under an inert atmosphere using a macro-thermogravimetric analysis (TGA) system at a constant heating rate of 5 °C min^{-1}. The corresponding TGA and derivative thermogravimetric (DTG) curves are shown in Fig. 2a. The overall thermal degradation process of rice straw can be divided into three distinct stages: (i) dehydration, (ii) devolatilization (release of volatile components), and (iii) char formation. Each peak observed in the DTG profile represents a predominant reaction associated with a specific stage of decomposition.

As illustrated in Fig. 2a, the first DTG peak at approximately 117 °C, within the dehydration region (below 220 °C), corresponds to the evaporation of physically adsorbed and bound H_2O molecules. The major mass loss occurring between 220 °C and 500 °C is primarily attributed to the decomposition of hemicellulose, cellulose, and partially lignin. This stage is characterized by the release of a substantial amount of volatile matter, leading to a pronounced mass reduction exceeding 40%. The second DTG peak, centered at 347 °C, represents the maximum rate of weight loss, with $R_{max} = 7.6\%/°C$.

The third stage of thermal decomposition, observed above 500 °C, is associated with the gradual degradation of residual lignin and the formation of a carbon-rich char. At this point, most volatile compounds had already been eliminated, resulting in only minor additional weight loss. Compared to a previous investigation conducted at an identical heating rate of 5 °C min^{-1}, the second DTG peak in the present study appeared at a slightly higher temperature, suggesting a shift in the decomposition kinetics of the biomass.[29] Nevertheless, lignin degradation and subsequent carbonization of rice straw were nearly complete at approximately 600 °C. These findings indicate that 600 °C represents an optimal temperature for the carbonization of rice straw, serving as a suitable condition for subsequent material synthesis processes.

3.2 FT-IR analysis

FT-IR spectroscopy was employed to elucidate the chemical evolution from pristine rice straw to carbonized rice straw and finally to NS-CQDs (Fig. 2b). The corresponding FT-IR band assignments are summarized in Table S1 (SI).

In the FT-IR spectrum of rice straw, the absorption bands in the regions of 3200–3500 cm^{-1} and 2850–2950 cm^{-1}, typically assigned to O–H and aliphatic C–H stretching vibrations, are relatively weak and poorly resolved. This may be attributed to the strong overlap of multiple vibrational modes, the heterogeneous nature of the lignocellulosic matrix, and the presence of a high inorganic (silica) content, which can suppress the intensity of organic functional group vibrations.

In contrast, distinct absorption features are observed in the fingerprint region. The strong band at ~1035 cm^{-1}, together with the bending vibration at ~459 cm^{-1}, can be clearly assigned to Si–O–Si stretching and bending modes, respectively, confirming the dominant contribution of silica in the rice straw sample. These features are consistent with the known silica-rich structure of rice straw and explain the relatively weak signals associated with organic components.[29–31]

After carbonization, significant changes in the FT-IR spectrum are observed. The intensity of the broad O–H band decreases markedly, indicating dehydration and structural

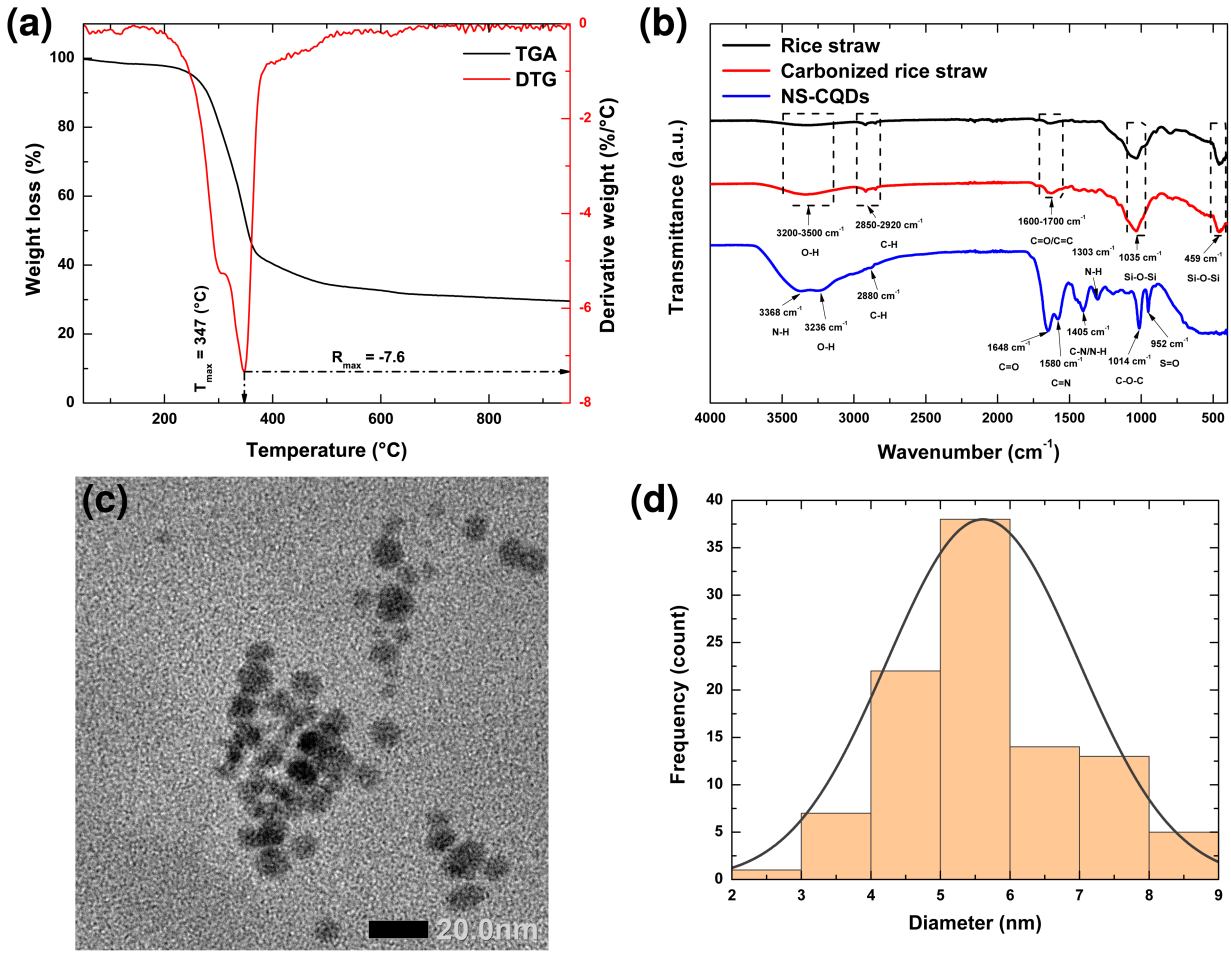

Fig. 2 (a) TGA-DTG analysis of rice straw; (b) FT-IR spectra of carbonized rice straw and respective NS-CQDs; (c) representative TEM image of the NS-CQDs; (d) size histogram of the NS-CQDs with curve fitted to the data using a Gaussian model.

decomposition of the lignocellulosic matrix. The aliphatic C–H stretching bands are also significantly weakened, suggesting the breakdown of polysaccharide chains. Meanwhile, absorption in the region of 1600–1700 cm^{-1} becomes more pronounced, which can be associated with the formation of C=O and conjugated C=C structures as a result of aromatization during carbonization. Notably, the Si–O–Si related bands remain visible, implying that silica is thermally stable and becomes relatively enriched after the removal of organic components.

In contrast, the FT-IR spectrum of NS-CQDs exhibits a markedly different vibrational profile. As shown by the blue trace, the hydrothermally synthesized NS-CQDs display a broad absorption band centered at approximately ~3368 cm^{-1}, accompanied by a shoulder near ~3236 cm^{-1}. These features are attributed to overlapping O–H and N–H stretching vibrations, reflecting the presence of hydrogen-bonded hydrophilic functional groups on the NS-CQD surface.[32] The band at ~2880 cm^{-1} corresponds to residual C–H stretching vibrations. A strong absorption at ~1648 cm^{-1} can be assigned to C=O stretching vibrations of amide and/or carboxyl groups, while the bands at ~1580 cm^{-1}, ~1405 cm^{-1} and ~1303 cm^{-1} are associated with C=N and C–N/N–H vibrations, respectively, confirming the successful incorporation of nitrogen-containing functionalities.[33,34]

The absorption band located at ~1014 cm^{-1} can be assigned to C–O–C stretching vibrations of ether or epoxy groups on the surface of NS-CQDs.[35] Although Si–O–Si stretching vibrations may appear in a similar spectral region, the absence of the characteristic Si–O–Si bending mode at ~459 cm^{-1} in the NS-CQDs spectrum suggests that silica has been effectively removed during the hydrothermal process. Therefore, the contribution of residual silica to this band is considered negligible.

Furthermore, the presence of a distinct band at ~952 cm^{-1} is attributed to S=O stretching vibrations, providing evidence for successful sulfur doping.[35] The coexistence of oxygen-, nitrogen-, and sulfur-containing functional groups confirms the highly functionalized nature of the NS-CQDs surface.

Overall, the FT-IR results clearly demonstrate the transformation of rice straw into heteroatom-doped carbon quantum dots, accompanied by the elimination of silica-related features and the formation of abundant surface functional groups. These functionalities are expected to enhance the aqueous

dispersibility and provide active sites for metal ion coordination and reactive oxygen species generation, which are beneficial for sensing and antibacterial applications.

3.3 XPS analysis

The XPS survey spectrum of the NS-CQDs (Fig. 3a) exhibits four characteristic peaks assigned to C 1s (284.9 eV), O 1s (531.6 eV), N 1s (400.2 eV), and S 2p (168.1 eV). Quantitative elemental analysis, obtained by averaging the results from three different measurement points, reveals atomic contents of C (63.32 ± 0.61%), O (26.24 ± 0.73%), N (6.82 ± 0.26%), and S (3.62 ± 0.15%). These values confirm the successful incorporation of nitrogen and sulfur into the carbon framework. The averaged atomic percentages further indicate effective heteroatom doping and the presence of abundant surface functional groups on the NS-CQDs surface.

The high-resolution C 1s spectrum (Fig. 3b) can be deconvoluted into three main components located at approximately 284.8, 286.6, and 288.7 eV, which are assigned to C–C/C=C, C–N/C–O, and C=O (or O–C=O) bonds, respectively. These carbon species are in good agreement with the FT-IR results, which reveal the presence of C–O, C–N, and carbonyl/carboxyl vibrations. Together, these features indicate that the NS-CQDs consist of a conjugated carbon core decorated with abundant oxygen- and nitrogen-containing surface functional groups.

The O 1s spectrum (Fig. 3c) is well fitted by two characteristic components. The peak centered at 531.3 eV is attributed to C=O species, including carbonyl and carboxyl groups, while the component at 533.0 eV corresponds to C–O bonds

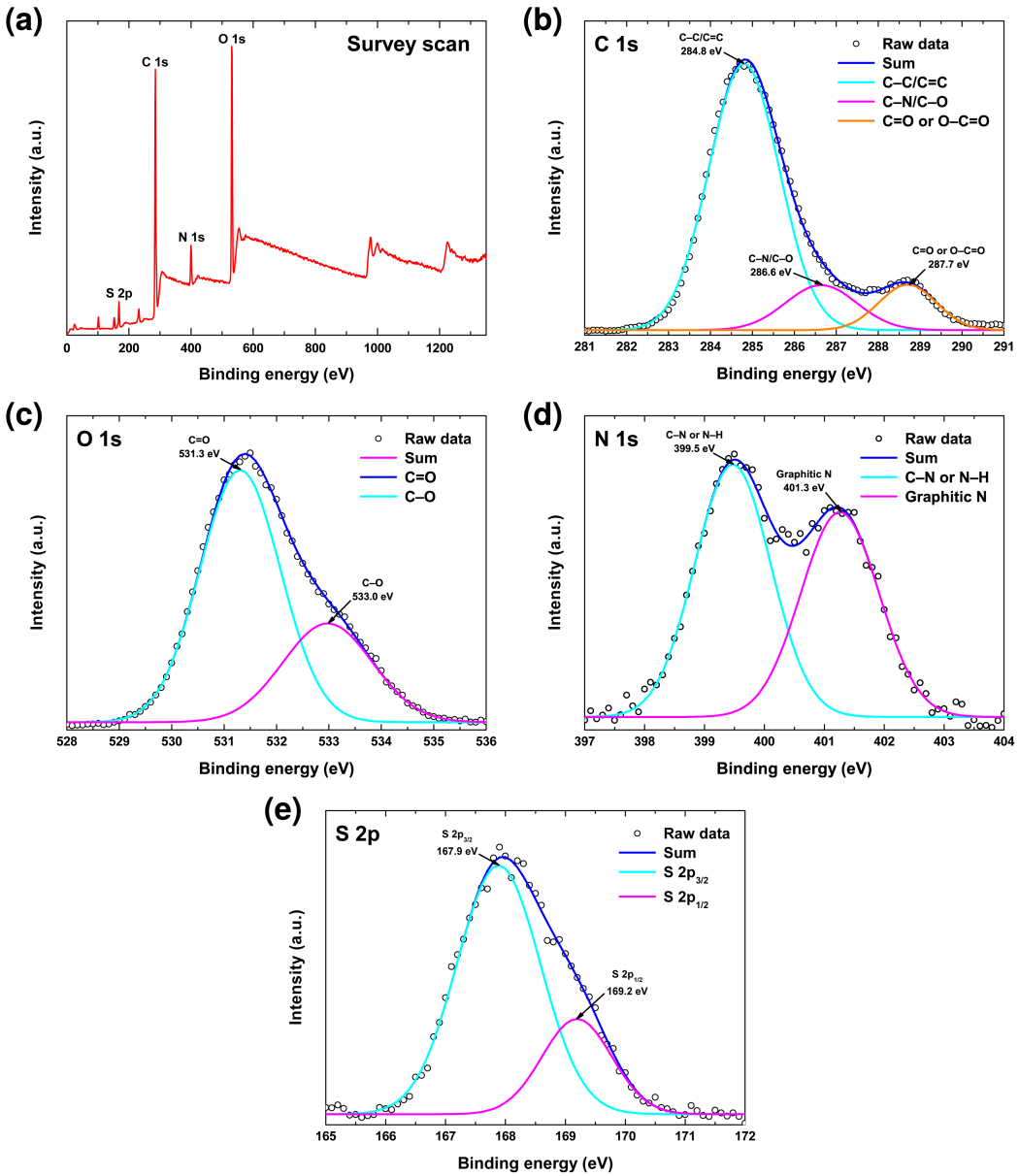

Fig. 3 (a) XPS survey spectra of NS-CQDs, (b) XPS graph of C 1s, (c) O 1s, (d) N 1s, (e) S 2p of NS-CQDs.

associated with hydroxyl and ether functionalities. This assignment is consistent with the FT-IR bands corresponding to O–H stretching and C=O/C–O vibrations. The coexistence of these oxygen-containing groups suggests partial oxidation of the carbon framework during synthesis and provides plentiful surface coordination sites for metal ions. In particular, the C=O and C–O moieties can interact effectively with Hg^{2+} through coordination and electron-transfer processes, which plays an important role in the fluorescence quenching mechanism of the NS-CQDs.

The high-resolution N 1s spectrum (Fig. 3d) can be deconvoluted into two components centered at approximately 399.5 and 401.3 eV. The lower binding energy peak at 399.5 eV is assigned to pyrrolic or amine-type nitrogen (C–N or N–H), whereas the peak at 401.3 eV corresponds to graphitic (quaternary) nitrogen incorporated into the carbon lattice. These assignments correlate well with the FT-IR signals associated with N–H bending and C–N stretching vibrations. Such nitrogen configurations modulate the electronic structure of the CQDs and introduce electron-donating sites on the surface, thereby facilitating coordination interactions with metal ions and contributing to the enhanced fluorescence response and selective sensing performance toward Hg^{2+}.

The S 2p spectrum (Fig. 3e) is deconvoluted into two peaks located at 167.9 and 169.2 eV, which are assigned to the S $2p_{3/2}$ and S $2p_{1/2}$ components of oxidized sulfur species (SO_x), respectively. The spin–orbit splitting of approximately 1.3 eV is characteristic of sulfur in high oxidation states, such as sulfonate or sulfate groups. This observation is consistent with the FT-IR bands attributed to S=O stretching vibrations. The absence of low-binding-energy signals associated with thiophene-like C–S–C bonds indicates that sulfur is predominantly present in oxygenated surface functionalities. These oxidized sulfur groups confirm successful sulfur incorporation and provide effective binding sites for Hg^{2+} through strong Hg–S interactions, thereby further enhancing the sensing performance of the NS-CQDs.

Collectively, the XPS results demonstrate that the NS-CQDs are enriched with oxygen-, nitrogen-, and sulfur-containing functional groups on their surface. These findings are fully consistent with the FT-IR analysis and confirm the successful heteroatom doping and surface functionalization of the CQDs. The synergistic presence of C=O, C–O, C–N, and SO_x groups plays a crucial role in regulating the photoluminescence properties and providing multiple coordination sites for Hg^{2+}, which underpins the high sensitivity and selectivity of the proposed sensing system.

3.4 EDX analysis

The elemental composition and spatial distribution of the NS-CQDs were further examined by EDX analysis (Fig. 4). The summed EDX spectrum (Fig. 4a) confirms the presence of C, O, N, and S as the principal constituent elements, consistent with successful nitrogen and sulfur co-doping of the carbon framework. A distinct Si Kα signal at 1.74 keV is also observed, which originates from the underlying silicon substrate used for sample support. Quantitative analysis indicates weight percentages of 30.78 ± 0.14% for C, 50.00 ± 0.17% for O, 12.30 ± 0.23% for N, and 6.01 ± 0.03% for S, further evidencing the effective incorporation of heteroatoms and the abundance of oxygen-containing surface functionalities.

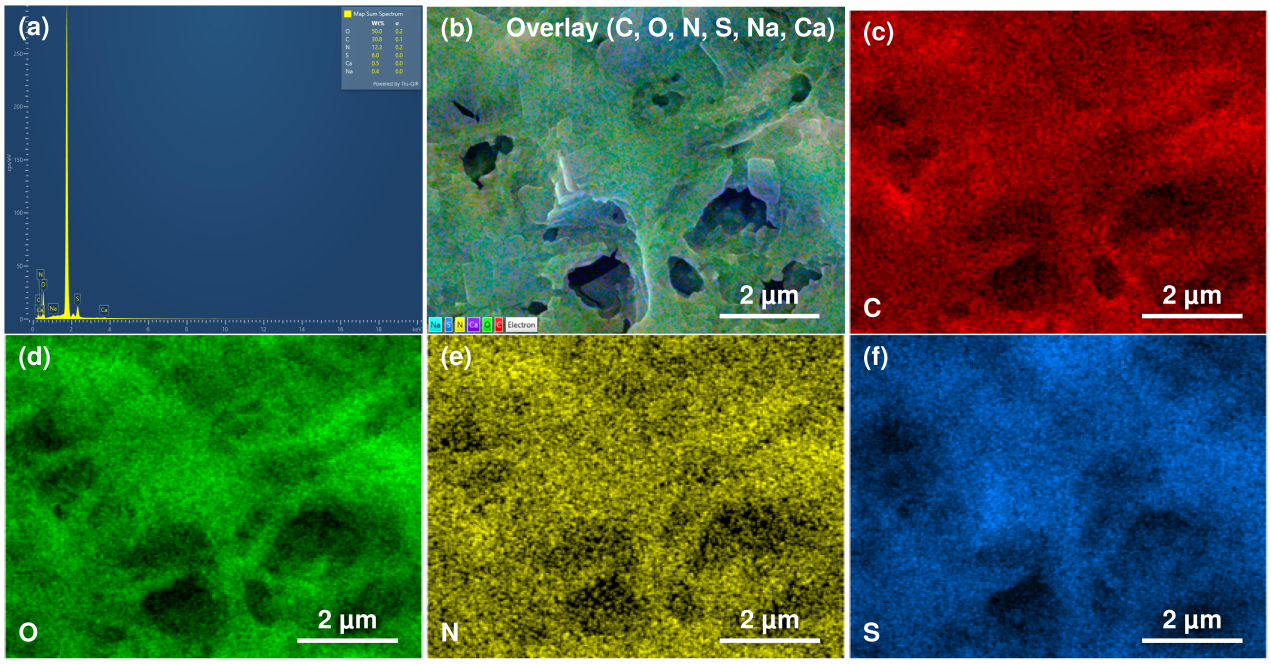

Fig. 4 EDX elemental mapping of NS-CQDs: (a) summed EDX spectrum; (b) composite overlay of all detected elements; (c–f) individual elemental maps of C, O, N, and S.

The corresponding elemental mapping images (Fig. 4c–f) reveal a homogeneous spatial distribution of C, O, N, and S across the analyzed region, indicating uniform heteroatom incorporation within the NS-CQDs. Weak signals of Na (0.37 ± 0.02 wt%) and Ca (0.55 ± 0.02 wt%) are also detected. These trace elements are attributed to residual inorganic components inherently present in rice straw and were not intentionally introduced during synthesis. Their low concentrations and non-uniform distributions suggest that they do not participate in the carbon framework or significantly influence the optical and sensing properties of the NS-CQDs. Overall, the EDX results are in good agreement with the FT-IR and XPS analyses, providing complementary evidence for the successful formation of N,S-co-doped carbon quantum dots with abundant surface functional groups.

3.5 Structural and optical characterization of NS-CQDs

The morphological characterization of the CQDs was analyzed using TEM, and the particle size distribution is shown in Fig. 2c and d. The results indicate that the CQDs are primarily monodispersed and spherical, with particle sizes ranging from 2 to 9 nm and the mean particle size of 5.61 ± 1.38 nm.

The optical characteristics of NS-CQDs play a pivotal role in determining their functional performance across diverse applications. Under ambient illumination, the well-dispersed NS-CQD solution exhibits a brown coloration; however, upon irradiation with ultraviolet (UV) light at 365 nm, it emits an intense blue fluorescence observable to the naked eye (Fig. 5a). This pronounced photoluminescence underscores the potential of NS-CQDs for use in optical sensing, bioimaging, and photonic devices.

The UV-Vis absorption spectrum of NS-CQDs displays two distinct shoulder peaks centered at approximately 243 nm and 333 nm (Fig. 5a), which can be attributed to the π → π* transition of conjugated C=C bonds within the aromatic sp^2 domains and the n → π* transition of carbonyl (C=O) groups, respectively.[36–38] These absorption features correspond closely to the two excitation peaks observed in the photoluminescence excitation (PLE) spectrum (Fig. 5b), confirming their origin from core and surface electronic transitions. In addition, the

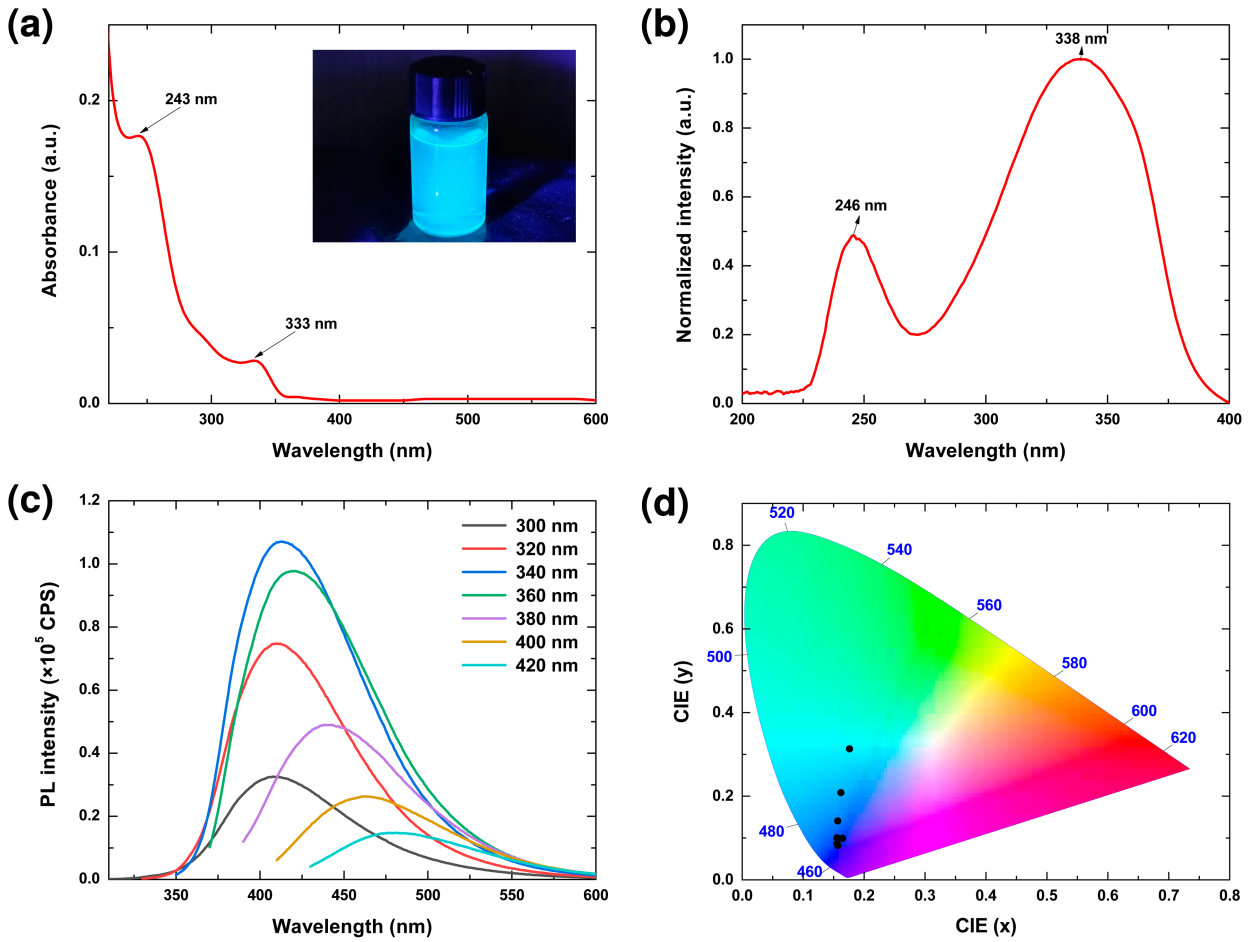

Fig. 5 (a) UV-Vis absorption spectrum of NS-CQDs, showing characteristic absorption bands associated with π → π* and n → π* electronic transitions. (b) PLE spectrum monitored at an emission wavelength of 430 nm, highlighting the main excitation bands corresponding to the UV-Vis absorption features. (c) PL emission spectra of NS-CQDs recorded at various excitation wavelengths, demonstrating excitation-dependent emission behavior indicative of multiple emissive surface states. (d) Commission Internationale de l'Éclairage (CIE) 1931 chromaticity coordinates derived from the PL spectra in (c), illustrating the variation in emission color with excitation wavelength.

absorption tail extending toward the visible region is commonly associated with n → π* transitions originating from surface functional groups such as C═O and C═N, in agreement with the FT-IR results.[39–41]

Furthermore, the PL spectra of NS-CQDs exhibit pronounced excitation-dependent emission behavior within the excitation wavelength range of 310–600 nm, a characteristic commonly associated with surface defect states and heterogeneous emissive sites.[42,43] As illustrated in Fig. 5c, the emission peak undergoes a progressive redshift from 408 nm to 477 nm as the excitation wavelength increases from 300 to 420 nm. The emission intensity reaches its maximum at an excitation wavelength of 340 nm, suggesting optimal excitation–emission coupling under these conditions.

To further elucidate the colorimetric characteristics of the emission, the corresponding Commission Internationale de l'Éclairage (CIE) 1931 chromaticity coordinates were calculated for the peak emission wavelengths at 408, 410, 413, 421, 439, 462, and 477 nm (Fig. 5d). All emission points are located within the blue region of the CIE diagram, confirming the strong blue luminescence of the NS-CQDs. A gradual shift of the chromaticity coordinates from deeper to lighter blue tones is observed with increasing excitation wavelength, consistent with the excitation-dependent emission behavior described above. This tunable emission originates from variations in surface defect states and the size distribution of carbon cores, which together govern the recombination dynamics of photogenerated charge carriers. These results confirm that the synthesized NS-CQDs possess stable and tunable blue fluorescence, making them promising candidates for applications in optoelectronic devices and fluorescent sensing.

The QY of the NS-CQDs was determined using quinine sulfate as a standard reference.[44] At an excitation wavelength of 320 nm, the QY was calculated to be approximately 39.7%, which is notably higher than that of undoped CQDs.[45,46] This enhancement can be ascribed to the synergistic effects of nitrogen and sulfur co-doping, which effectively modulate surface states and promote radiative recombination efficiency.

The PL stability of the synthesized NS-CQDs was systematically evaluated under various environmental conditions to determine the optimal parameters for sensing applications. As illustrated in Fig. 6a, the fluorescence intensity of NS-CQDs

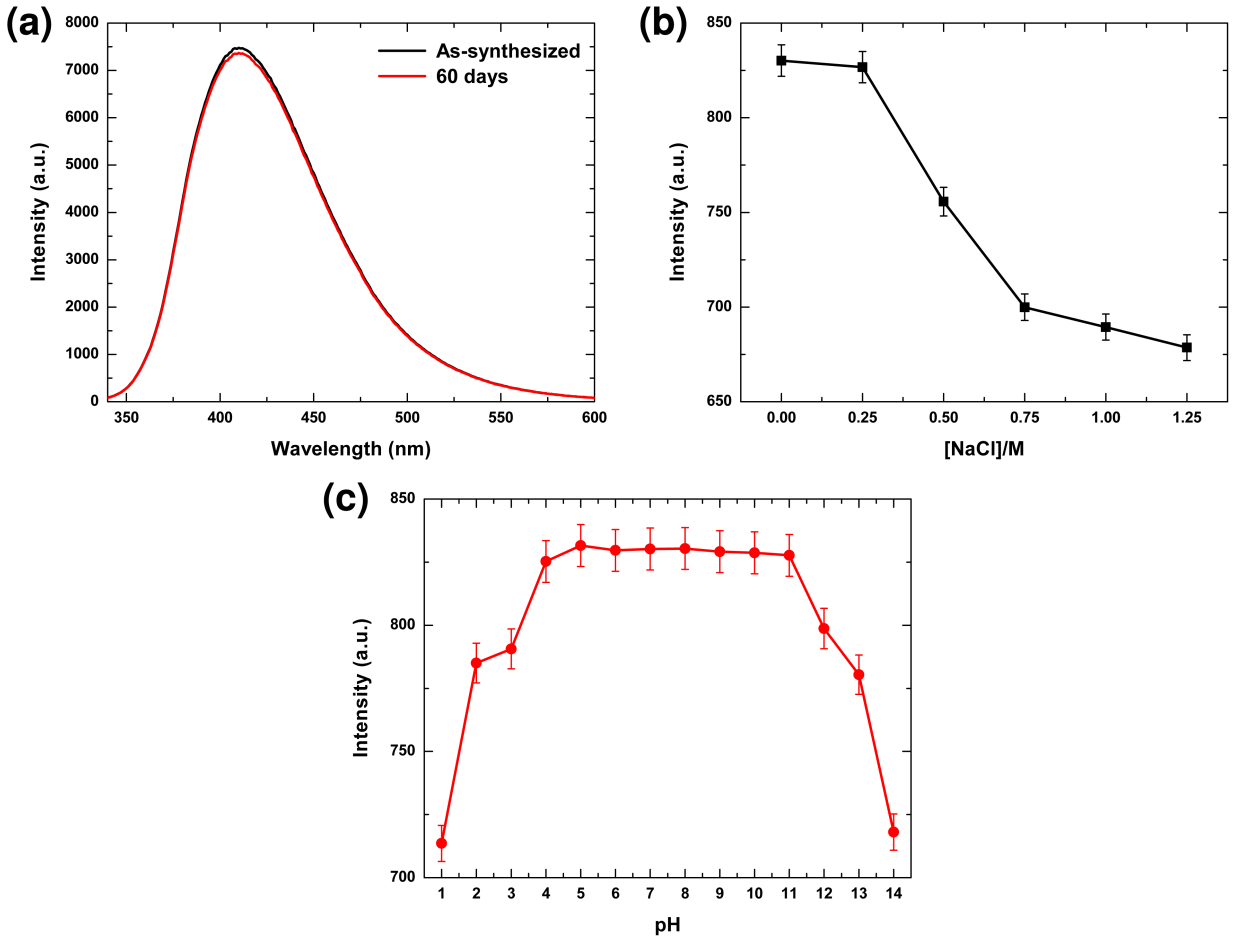

Fig. 6 (a) PL spectra of NS-CQDs monitored over 60 days, demonstrating their temporal fluorescence stability during storage. (b) Fluorescence intensity of NS-CQDs at 426 nm under varying NaCl concentrations (0–1.25 M), measured in 50 mM NaAc–HAc buffer solution at pH 5.0 and an excitation wavelength of 340 nm, indicating excellent stability under high-ionic-strength conditions. (c) Fluorescence intensity of NS-CQDs at 426 nm as a function of pH, showing the dependence of emission behavior on the protonation and deprotonation of surface functional groups.

stored at 4 °C exhibited excellent temporal stability, with only a marginal decrease of approximately 5% after 60 days compared to the initial emission value. This result indicates the robust chemical stability and resistance to photobleaching of the NS-CQD structure under ambient storage conditions.

To assess the ionic stability, the fluorescence response of NS-CQDs was examined in solutions containing NaCl concentrations ranging from 0 to 1.25 M (Fig. 6b). The negligible variation in PL intensity across this concentration range suggests that the NS-CQDs possess high colloidal stability and strong surface passivation, preventing aggregation even under high-ionic-strength conditions. This behavior is essential for reliable fluorescence sensing in complex aqueous or biological environments.

The effect of pH on the PL characteristics of NS-CQDs was systematically examined over a broad pH range of 1–14 (Fig. 6c). A noticeable decrease in fluorescence intensity was observed under strongly acidic conditions (pH $\leq$ 3), where the emission intensity retained only 85.95%, 94.56%, and 95.24% of its value at neutral pH (pH ~7) at pH values of approximately 1, 2, and 3, respectively. This reduction is attributed to the protonation of surface functional groups, which promotes nonradiative recombination pathways and consequently quenches the fluorescence emission. As the pH increased, the PL intensity rose rapidly and remained nearly constant and maximal within the range of pH 4–11, indicating excellent fluorescence stability across a wide pH window. However, a significant decrease in fluorescence intensity was observed again under highly basic conditions (pH $\geq$ 12), likely resulting from the deprotonation and disruption of surface passivation layers. This pH-dependent fluorescence behavior can be attributed to the reversible protonation and deprotonation of surface groups such as –COOH, –OH, and –NH_2, which modulate the surface charge distribution and electronic states of the NS-CQDs.[47–49]

At elevated pH values, Hg^{2+} ions are prone to hydrolysis, forming species such as $Hg(OH)^+$, $Hg(OH)_2$, and colloidal HgO, which significantly reduce the concentration of free Hg^{2+} available for interaction with the surface functional groups of NS-CQDs.[50,51] This transformation diminishes the fluorescence quenching efficiency, thereby compromising both detection sensitivity and reproducibility. In contrast, under mildly acidic conditions (around pH ~5), Hg^{2+} ions remain predominantly in their free ionic form, enabling strong coordination with donor functional groups such as –COOH, –OH, and –NH_2 on the NS-CQD surface.[52,53] These interactions facilitate efficient charge transfer and nonradiative recombination, resulting in a more pronounced and stable fluorescence response. To further enhance sensing stability and maintain a consistent microenvironment, an HAc–NaAc buffer system was employed, as it provides a high complexation stability constant for Hg^{2+} ions ($\log K = 8.43$).[54] Therefore, pH ~5 was identified as the optimal working condition for Hg^{2+} detection, offering both ionic stability and reliable fluorescence response.

3.6 Fluorescence sensing performance toward Hg^{2+} ions

The selectivity and recognition capability of the synthesized NS-CQDs toward various metal ions were systematically evaluated using a series of representative cations at a concentration of 200 μM. The corresponding fluorescence responses are shown in Fig. 7a. Upon addition of different metal ions, the PL intensity of NS-CQDs decreased to varying extents ($I/I_0 < 1$), indicating fluorescence quenching arising from interactions between metal ions and surface functional groups of the CQDs. This quenching behavior is mainly attributed to nonradiative decay pathways and/or electron or energy transfer processes that inhibit radiative recombination.

Among all tested species, Hg^{2+} produced the most significant quenching effect ($I/I_0 = 0.285$), reflecting its strong affinity toward sulfur- and nitrogen-containing functional groups on the NS-CQDs surface. Importantly, other toxic heavy metal ions with similar environmental relevance, including Pd^{2+}, Cd^{2+}, and Pb^{2+}, induced only moderate or weak quenching, with I/I_0 values

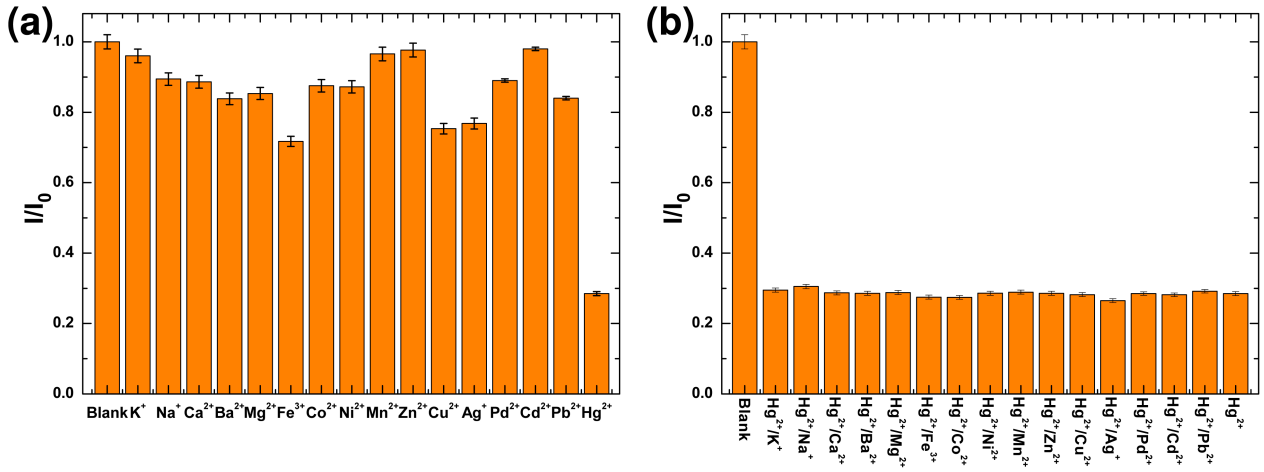

Fig. 7 (a) Comparative PL responses of NS-CQDs in the presence of various metal ions, illustrating their selective fluorescence behavior. (b) Photoluminescence intensity comparison of NS-CQDs exposed to individual metal ions and to mixtures containing Hg^{2+}, demonstrating the pronounced fluorescence quenching effect induced by mercury ions.

of 0.891, 0.978, and 0.839, respectively. This clear contrast demonstrates that the NS-CQDs exhibit much stronger interaction with Hg^{2+} than with other heavy metals of comparable chemical nature. In comparison, common metal ions such as Mn^{2+} (I/I_0 = 0.966), Zn^{2+} (I/I_0 = 0.977), and K^+ (I/I_0 = 0.960) caused only negligible fluorescence suppression, indicating weak nonspecific interactions.

To further assess the anti-interference capability, competitive experiments were carried out by introducing Hg^{2+} into solutions containing other metal ions (Fig. 7b). The PL response toward Hg^{2+} remained essentially unchanged in the presence of coexisting ions, confirming the selective recognition of Hg^{2+} by NS-CQDs. Although Fe^{3+}, Cu^{2+}, and Ag^+ exhibited moderate quenching in single-ion systems (Fig. 7a), they did not significantly interfere with the Hg^{2+}–NS-CQDs interaction under mixed-ion conditions, consistent with previous reports.[55–57] These results demonstrate that the NS-CQDs possess high selectivity and strong resistance to interference for Hg^{2+} detection, even in the presence of other toxic heavy metal ions.

The fluorescence quenching mechanism and selectivity toward Hg^{2+} were elucidated through PL and UV-Vis absorption analyses. Upon the introduction of Hg^{2+} ions, the characteristic absorption band of NS-CQDs centered at 333 nm gradually diminished (Fig. S1, SI), accompanied by a pronounced decrease in emission intensity. This attenuation, corresponding to n → π* transitions of surface carbonyl and imine moieties, indicates that strong coordination occurs between Hg^{2+} ions and the surface functional groups (–COOH, –OH, $–NH_2$) of the CQDs. Such coordination perturbs the surface electronic states, leading to both static quenching (ground-state complex formation) and dynamic quenching (collisional or electron/energy transfer), which together account for the observed fluorescence suppression.[51,58–61]

The pronounced selectivity toward Hg^{2+} is primarily attributed to the high affinity of mercury ions for oxygen- and nitrogen-containing donor groups on the CQD surface. To substantiate this hypothesis, an acetate buffer system (HAc–NaAc) was employed to provide a consistent microenvironment, as acetate shares structural similarity with the carboxylate groups present on CQDs. The complexation stability constant ($\log K_F$) of Hg^{2+} with acetate (8.43) is significantly higher than those of other competing ions such as Ag^+, Cd^{2+}, Co^{2+}, Cu^{2+}, Ni^{2+}, and Pb^{2+}.[54,57] This strong binding affinity promotes the formation of non-emissive surface complexes and efficient charge transfer from excited CQDs to Hg^{2+}, resulting in distinct fluorescence quenching. Moreover, when Hg^{2+} was introduced together with other metal ions, the emission intensity remained nearly unchanged compared with that of the single-ion condition, confirming the robustness and selectivity of the sensing system. These findings are consistent with previous reports, where Hg^{2+}–CQD interactions induced marked changes in both absorption and emission spectra, unlike other metal ions that mainly caused inner-filter effects or minor perturbations.[55,60]

Under the optimized synthesis and sensing conditions (200 °C for 8 h, pH = 5), the fluorescence response of nitrogen and sulfur co-doped carbon quantum dots (NS-CQDs) toward Hg^{2+} ions was systematically investigated. As illustrated in Fig. 8a, a gradual attenuation of fluorescence intensity was observed with increasing Hg^{2+} concentration. This quenching behavior is primarily attributed to the formation of non-emissive coordination complexes between Hg^{2+} ions and oxygen-containing functional groups (–OH and –COOH) present on the CQD surface, which facilitate efficient electron or energy transfer processes.[62,63] As shown in Fig. 8b, the fluorescence intensity exhibited a linear correlation with Hg^{2+} concentration within the range of 0–100 μM, consistent with the Stern–Volmer relationship:

$$\frac{I_0}{I} = 1 + K_{SV}C, \tag{2}$$

where K_{SV} is the Stern–Volmer constant, C is the concentration of Hg^{2+} (μM), and I_0 and I represent the PL intensities of NS-CQDs in the absence and presence of Hg^{2+}, respectively.[64]

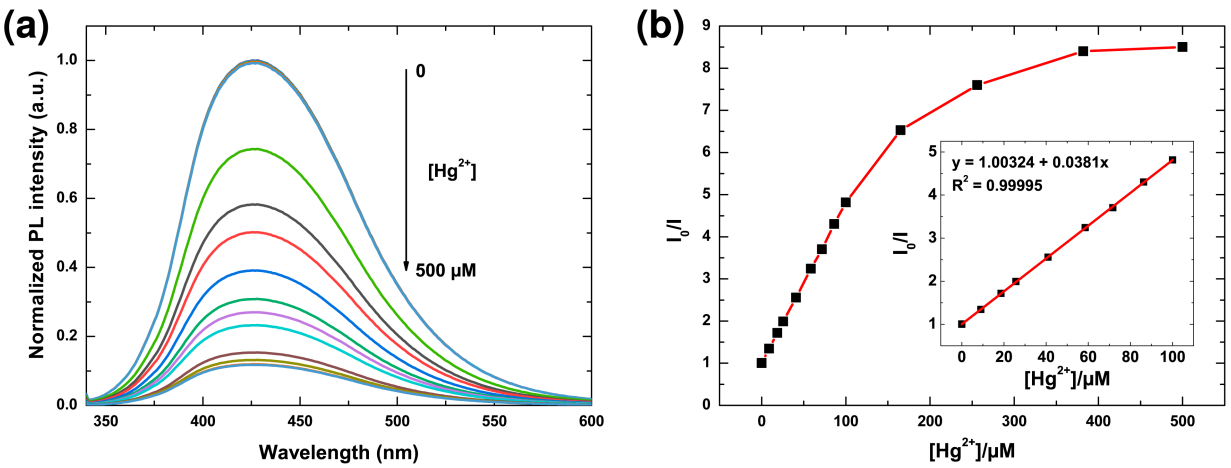

Fig. 8 (a) Fluorescence emission spectra of NS-CQDs in the presence of various concentrations of Hg^{2+}; (b) plot of I_0/I *versus* Hg^{2+} concentration in a pH 5.0 buffer solution (50 mM NaAc-HAc), where I_0 and I represent the fluorescence intensities of NS-CQDs at 426 nm in the absence and presence of Hg^{2+}, respectively (excitation wavelength: λ_{ex} = 340 nm).

As depicted in Fig. 8b, a linear relationship between I_0/I and Hg^{2+} concentration is observed over 0–100 μM range ($R^2 \approx 0.99995$), confirming that the quenching follows the Stern–Volmer behavior.

The fluorescence quenching effect of green-synthesized NS-CQDs derived from rice straw, applied as a fluorescent probe for Hg^{2+} ions, has shown great potential. The experiment was performed in triplicate, and the limit of detection (LOD) was calculated using the following equation:[57,65]

$$\mathrm{LOD} = \frac{3.3\sigma}{K_{\mathrm{SV}}}, \tag{3}$$

where σ represents the standard deviation of the blank signal. In this study, σ was determined from the statistical deviation of the PL intensity ratio obtained through ten independent measurements of the blank sample in the absence of Hg^{2+} ions. All measurements were conducted under identical experimental conditions to ensure the precision of background noise estimation and the reliability of the calculated detection limit. The resulting value of σ was found to be 0.00171. The factor of 3.3, rather than 3, is adopted to account for the limited number of blank measurements, as recommended by IUPAC. This adjustment provides a confidence level close to 99%, offering a practical balance between statistical reliability and analytical sensitivity when estimating the detection limit from a small sample set.[66,67] Based on the obtained Stern–Volmer constant ($K_{\mathrm{SV}} = 0.0381\ \mu M^{-1}$), the limit of detection (LOD) for Hg^{2+} was calculated to be 0.148 μM within the investigated concentration range, corresponding to approximately 29.7 μg L^{-1} of mercury. International regulatory authorities, including the FAO/WHO Codex Alimentarius Commission, the European Commission, and the U.S. Food and Drug Administration (FDA), have established maximum permissible mercury levels in food products typically in the range of 0.5–1.0 mg kg^{-1}, depending on the food matrix and mercury species.[68–70] Although these regulatory limits are expressed on a mass-per-mass basis, the detection capability achieved in this study is sufficiently low to enable reliable mercury determination following appropriate sample extraction or dilution procedures. These results indicate that the proposed NS-CQDs-based fluorescent sensor provides adequate sensitivity for practical applications in food safety and environmental monitoring.

The fluorescence quenching behavior of NS-CQDs toward Hg^{2+} ions suggests the coexistence of both static and dynamic

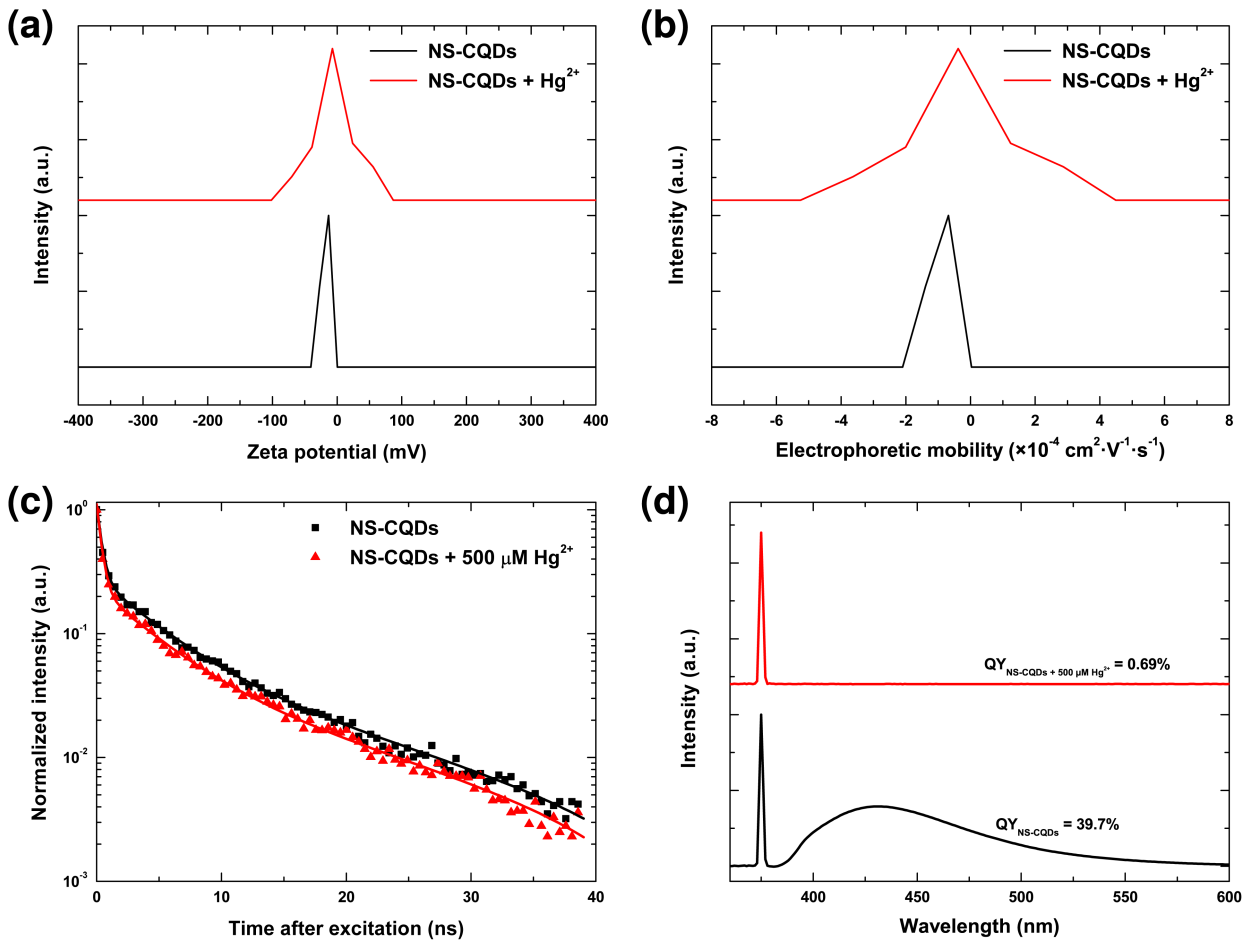

Fig. 9 Zeta potential (a) and electrophoretic mobility (b) of NS-CQDs measured in the absence and presence of 500 μM Hg^{2+} ions; (c) photoluminescence (PL) decay curves of NS-CQDs in the absence and presence of 500 μM Hg^{2+} ions, measured at room temperature; (d) QY curves of NS-CQDs in the absence and presence of 500 μM Hg^{2+} ions.

quenching mechanisms. To further elucidate the underlying processes, comparative analyses were conducted between pristine NS-CQDs and those exposed to Hg^{2+} ions in aqueous solution. The surface complexation and charge redistribution upon metal ion binding were examined through zeta potential and electrophoretic mobility measurements. As shown in Fig. 9a, the mean zeta potential of NS-CQDs shifted from −15.9 mV to −7.7 mV after the addition of Hg^{2+} ions, indicating a partial neutralization of surface charges due to coordination between Hg^{2+} and negatively charged surface groups.[72] The negative zeta potential values reflect the abundance of deprotonated carboxyl (–COOH) and hydroxyl (–OH) groups on the NS-CQD surface, which confer colloidal stability by generating electrostatic repulsion among particles. Upon exposure to Hg^{2+}, these negatively charged groups interact or form coordination complexes with the cationic mercury species, thereby reducing the magnitude of the negative potential.

A consistent trend was observed in electrophoretic mobility measurements (Fig. 9b). The average mobility of NS-CQDs changed from -8.2×10^{-5} to -4.0×10^{-5} $cm^2 \cdot V^{-1} \cdot s^{-1}$ upon complexation with Hg^{2+}, indicating a decrease in the absolute value of electrophoretic mobility and confirming the reduction in surface charge and electrostatic driving force.[73] The negative sign of electrophoretic mobility reflects the net negative surface charge of NS-CQDs, which causes them to migrate toward the anode under an applied electric field. The smaller magnitude of mobility after Hg^{2+} binding signifies partial neutralization of negatively charged sites and reduced electrostatic responsiveness, consistent with the zeta potential measurements.

The time-resolved photoluminescence (TRPL) decay profiles of the NS-CQDs are presented in Fig. 9c, where the normalized fluorescence intensity is plotted as a function of time. The decay curves were well fitted using a tri-exponential function:[74,75]

$$I(t) = A_1 \exp(-t/\tau_1) + A_2 \exp(-t/\tau_2) + A_3 \exp(-t/\tau_3), \quad (4)$$

where $I(t)$ is the fluorescence intensity at time t, and A_i and τ_i (i = 1, 2, 3) represent the pre-exponential amplitudes and corresponding decay time constants, respectively. The average fluorescence lifetime (τ_{avg}) was determined using the weighted expression:

$$\tau_{avg} = \frac{A_1\tau_1^2 + A_2\tau_2^2 + A_3\tau_3^2}{A_1\tau_1 + A_2\tau_2 + A_3\tau_3}, \quad (5)$$

The TRPL results further substantiate that the fluorescence quenching of NS-CQDs by Hg^{2+} is predominantly governed by a static quenching mechanism. As shown in Fig. 9c and Table 1, the average lifetime increased slightly from 10.40 ns (0 μM Hg^{2+}) to 11.36 ns (500 μM Hg^{2+}), indicating the formation of ground-state complexes between Hg^{2+} ions and the surface functional groups of NS-CQDs rather than collisional (dynamic) deactivation.[76] Moreover, the quenching process occurred rapidly—within 2 minutes after ion introduction—and the fluorescence signal remained stable for up to 20 minutes (Fig. S2), confirming the fast response and excellent temporal stability of the NS-CQD-based mercury sensor.

As illustrated in Fig. 9d, the NS-CQDs exhibit intense blue fluorescence with a high quantum yield (QY) of 39.7%, which is higher than or comparable to most biomass-derived CQD probes reported to date (Table 2). In particular, this QY is markedly higher than those reported for bamboo cellulose-derived S-CQDs (1.5%),[23] lemon peel-derived N,S-CQDs (15.2%),[24] and lotus root-derived N-CQDs (19.0%),[71] and is slightly higher than that of wheatgrass-derived N,Cl-CQDs (36%).[22] The enhanced fluorescence efficiency is attributed to the synergistic effect of nitrogen and sulfur co-doping introduced from independent dopant sources (gelatin and DMSO). This dual-dopant strategy effectively passivates surface defects while simultaneously generating electron-rich surface states, thereby suppressing nonradiative recombination pathways and increasing the probability of radiative transitions.

Upon the addition of Hg^{2+}, the quantum yield decreases sharply from 39.7% (0 μM) to 0.69% (500 μM), indicating highly efficient fluorescence quenching induced by strong complexation between mercury ions and surface functional groups of the NS-CQDs. Compared with previously reported biomass-derived CQDs (Table 2), the present NS-CQDs exhibit a substantially wider linear detection range (0–100 μM), which is markedly broader than those of bamboo cellulose–derived CQDs (0.0005–0.001 μM)[23] and wheatgrass-derived CQDs (0–0.35 μM).[22] This expanded linearity implies a higher density and greater chemical diversity of accessible coordination sites for Hg^{2+} on the NS-CQD surface, enabling progressive complex formation without rapid saturation of the fluorescence response. In addition, the NS-CQDs demonstrate excellent selectivity against 16 potentially interfering metal ions, a short response time of approximately 2 min, and reliable analytical performance in real river water samples (Table S3), underscoring their practical applicability for environmental mercury monitoring.

In comparison with non-biomass-derived CQDs (Table S2), the present NS-CQDs also show competitive or superior sensing performance. For example, citric-acid-derived NS-CQDs typically exhibit quantum yields of 10–37% and limits of detection of 0.16–0.29 μM,[64,77] whereas the rice straw–derived NS-CQDs achieve a higher quantum yield (39.7%) together with

Table 1 Fitting parameters of the corresponding PL decay curves to a triple-exponential function. The excitation and emission wavelengths are 375 nm and 430 nm, respectively

Hg^{2+} added (μM)	A_1 (%)	τ_1 (ns)	A_2 (%)	τ_2 (ns)	A_3 (%)	τ_3 (ns)	τ_{avg} (ns)	Adj. R^2
0	82.691	0.37522	23.301	4.4751	5.489	20.06124	10.95009	0.99398
500	87.941	0.36405	19.356	4.42336	4.232	21.6728	11.35973	0.99398

Table 2 Comparison of analytical performance of representative biomass-derived carbon quantum dot (CQD)–based fluorescent sensors for Hg^{2+} detection with the NS-CQDs developed in this work. References are listed in order of increasing LOD values

Ref.	Biomass precursor	Dopants	Synthesis method	QY (%)	Linear range (μM)	LOD (μM)
23	Bamboo cellulose	S	Hydrothermal	1.5	0.0005–0.001	0.00516
24	Waste lemon peel	N, S	Hydrothermal	15.2	0.0176–20	0.0176
71	Lotus root	N	Microwave-assisted	19.0	0.1–60.0	0.0187
22	Wheatgrass	N, Cl	Microwave-assisted	36	0–0.35	0.039
This work	Rice straw	N, S	Hydrothermal	39.7	0–100	0.148

Table 3 Application of Hg^{2+} detection in real samples

Sample	Spike (μM)	Found (μM)	Recovery (%)	RSD, $n = 3$ (%)
Aqueous media	0	ND	—	—
	1	0.999 ± 0.014	99.86	1.42
	2	1.921 ± 0.015	96.04	3.94
	3	3.049 ± 0.045	101.62	1.48
To Lich river water	0	ND	—	—
	1	1.013 ± 0.002	101.34	1.78
	2	2.062 ± 0.055	103.1	2.67
	3	3.152 ± 0.1097	105.07	3.48

a comparable detection limit (0.148 μM), while benefiting from a renewable and low-cost precursor. This comparison highlights that both biomass selection and dopant chemistry play decisive roles in governing the optical and sensing properties of CQDs.

Overall, the quantitative comparisons in Tables 2, S2, and S3, together with spectroscopic and electrokinetic analyses, demonstrate that the superior sensing performance of the present NS-CQDs originates from (i) synergistic N,S co-doping using independent dopant sources, (ii) a high density of surface coordination sites for Hg^{2+}, and (iii) effective modulation of surface electronic states. These features collectively distinguish the present system from previously reported biomass-derived CQDs and account for its enhanced fluorescence efficiency, broad linear response, and robust analytical performance.

To further assess practical applicability, the NS-CQDs were applied to the determination of Hg^{2+} in environmental water samples, including river water collected from the To Lich River (Hanoi, Vietnam). Quantitative analysis using the standard addition method (Table 3) yielded recovery values of 96.04–101.62% for spiked aqueous samples and 101.34–105.07% for river water, with relative standard deviations (RSDs) below 3.5%. These results confirm that the NS-CQD probe maintains high analytical accuracy and reproducibility even in complex natural water matrices, demonstrating its robustness against matrix effects.

Taken together with the comparative performance analysis and mechanistic investigations, these practical tests further substantiate that the fluorescence quenching of NS-CQDs by Hg^{2+} is governed predominantly by static complex formation. This conclusion is consistently supported by the observed changes in zeta potential, fluorescence lifetime, and UV-Vis absorption spectra upon mercury binding. The strong coordination between Hg^{2+} and surface N-, O-, and S-containing functional groups underlies both the high selectivity and the efficient quenching response.

Collectively, the excellent sensitivity, broad linear range, strong anti-interference capability, and reliable real-sample performance establish the rice straw-derived NS-CQDs as a promising and sustainable fluorescent platform for trace-level Hg^{2+} monitoring in environmental and analytical applications.[58,78]

4 Conclusions

In this study, nitrogen and sulfur co-doped carbon quantum dots (NS-CQDs) were successfully synthesized from rice straw *via* a simple and sustainable hydrothermal route. Benefiting from the use of independent N and S dopant sources (gelatin and DMSO), the resulting NS-CQDs exhibit a high quantum yield (39.7%), good photostability, and strong affinity toward Hg^{2+}, enabling sensitive detection with a low limit of detection of 0.148 μM over a wide linear range. Compared with previously reported biomass-derived CQD probes, the present system achieves superior or comparable fluorescence efficiency while maintaining a broader working range, highlighting the effectiveness of controlled heteroatom co-doping and surface-state engineering.

Mechanistic investigations combining steady-state and time-resolved fluorescence spectroscopy, UV-Vis absorption, zeta potential, and electrophoretic mobility analyses demonstrate that fluorescence quenching is dominated by static complex formation between Hg^{2+} and surface O-, N-, and S-containing functional groups, with a minor contribution from dynamic processes. The synergistic interaction of multiple binding sites

not only enhances selectivity toward Hg^{2+} but also suppresses nonradiative recombination pathways, thereby accounting for the improved sensing performance. Furthermore, the nanosensor shows high accuracy and reproducibility in real water samples, confirming its robustness against matrix effects and its practical applicability for environmental analysis.

Overall, this work provides a clear structure–property–function correlation linking biomass precursor selection, heteroatom co-doping, and sensing performance. Beyond offering an efficient fluorescent probe for mercury detection, this study demonstrates a viable strategy for converting agricultural waste into high-value functional nanomaterials. The integration of sustainable feedstocks with rational surface chemistry design advances green nanotechnology and contributes to the development of cost-effective and environmentally benign platforms for heavy-metal monitoring.

Author contributions

Duc Cuong Nguyen: conceptualization, data curation, formal analysis, investigation, methodology, visualisation, writing – original draft, writing – review & editing. Bao Long Hoang: data curation, formal analysis, investigation, writing – review & editing. Van Duong Pham: data curation, formal analysis, methodology, writing – review & editing. Hop Bao Tung Nguyen: data curation, investigation, validation, writing – review & editing. Tuan Anh Pham: formal analysis, investigation, methodology, writing – review & editing. Thi Thao Vu: conceptualization, funding acquisition, investigation, project administration, supervision, writing – original draft, writing – review & editing.

Conflicts of interest

There are no conflicts of interest to declare.

Data availability

The data supporting the findings of this study are available within the article and its supplementary information (SI). Additional data are available from the corresponding author upon reasonable request. Please contact the corresponding author, Thi Thao Vu, at vtthao@vnu.edu.vn. Supplementary information is available. See DOI: https://doi.org/10.1039/d5ra09779g.

Acknowledgements

This research was funded by the research project QG.23.38 of Vietnam National University, Hanoi.

References

1 R. Janani, B. Gurunathan, K. Sivakumar, S. Varjani, H. H. Ngo and E. Gnansounou, *Environ. Res.*, 2022, **203**, 111815.
2 S. Rajendran, T. Priya, K. S. Khoo, T. K. Hoang, H.-S. Ng, H. S. H. Munawaroh, C. Karaman, Y. Orooji and P. L. Show, *Chemosphere*, 2022, **287**, 132369.
3 H. Hu, J. Zhao, L. Wang, L. Shang, L. Cui, Y. Gao, B. Li and Y.-F. Li, *TrAC, Trends Anal. Chem.*, 2020, **122**, 115721.
4 A. Alengebawy, S. T. Abdelkhalek, S. R. Qureshi and M.-Q. Wang, *Toxics*, 2021, **9**, 42.
5 M. Zaynab, R. Al-Yahyai, A. Ameen, Y. Sharif, L. Ali, M. Fatima, K. A. Khan and S. Li, *J. King Saud Univ., Sci.*, 2022, **34**, 101653.
6 E. Climent, M. D. Marcos, R. Martinez-Manez, F. Sancenón, J. Soto, K. Rurack and P. Amorós, *Angew. Chem., Int. Ed. Engl.*, 2009, **48**, 8519–8522.
7 W. Jung, C. S. Dunham, K. A. Perrotta, Y. Chen, J. K. Gimzewski and J. A. Loo, *J. Chem. Educ.*, 2022, **99**, 3566–3572.
8 D. L. F. da Silva, M. A. P. da Costa, L. O. B. Silva and W. N. L. Dos Santos, *Food Chem.*, 2019, **273**, 24–30.
9 A. Moutcine and A. Chtaini, *Sens. Bio-Sens. Res.*, 2018, **17**, 30–35.
10 S. Masha and O. S. Oluwafemi, *Mater. Lett.*, 2021, **283**, 128790.
11 M. Pajewska-Szmyt, B. Buszewski and R. Gadzała-Kopciuch, *Spectrochim. Acta, Part A*, 2020, **236**, 118320.
12 D. Yao, A. Liang and Z. Jiang, *Microchim. Acta*, 2019, **186**, 1–9.
13 R. Liu, J. Zhang, M. Gao, Z. Li, J. Chen, D. Wu and P. Liu, *RSC Adv.*, 2015, **5**, 4428–4433.
14 G. Somaraj, S. Mathew, T. Abraham, K. Ambady, C. Mohan and B. Mathew, *ChemistrySelect*, 2022, **7**, e202200473.
15 X. Yang, Y. Wang, J. Xu and M.-X. Zhao, *Microchem. J.*, 2021, **165**, 106033.
16 W. U. Khan, L. Qin, L. Chen, W. U. Khan, S. Zeb, A. Khan, S. Li, S. U. Khan, S. Kamal and P. Zhou, *Anal. Chim. Acta*, 2023, **1245**, 340847.
17 K. Liu, C. Xia, Y. Guo, H. Yu, Y. Xie and W. Yao, *Spectrochim. Acta, Part A*, 2023, **292**, 122395.
18 H. Wu and C. Tong, *J. Agric. Food Chem.*, 2019, **67**, 2794–2800.
19 N. Jaswal, J. Kour and P. Kumar, *J. Fluoresc.*, 2025, 1–14.
20 S. Liang, H. Feng, N. Chen, B. Wang, M. Hu, X. Huang, K. Yang and Y. Gu, *Bull. Chem. Soc. Jpn.*, 2024, **97**, uoae054.
21 R. Sharma and D. Singh, *ChemistrySelect*, 2025, **10**, e202405850.
22 S. Khare, N. Sohal, M. Kaur and B. Maity, *Heliyon*, 2025, **11**, year.
23 V. Bavya, T. P. D. Rajan and K. I. Suresh, *Langmuir*, 2025, **41**, 1333–1343.
24 Y. Pan, S. Guo, T. Wang, J. Lin, Z. Jia, F. Xu, R. Huang, H. Wang, C. Bai and J. Chen, *RSC Adv.*, 2026, **16**, 2652–2662.
25 P. Binod, R. Sindhu, R. R. Singhania, S. Vikram, L. Devi, S. Nagalakshmi, N. Kurien, R. K. Sukumaran and A. Pandey, *Bioresour. Technol.*, 2010, **101**, 4767–4774.
26 S. Bhuvaneshwari, H. Hettiarachchi and J. N. Meegoda, *Int. J. Environ. Res. Public Health*, 2019, **16**, 832.
27 Y. Li, Y. Liu, X. Shang, D. Chao, L. Zhou and H. Zhang, *Chem. Phys. Lett.*, 2018, **705**, 1–6.

28 G. A. Crosby and J. N. Demas, *J. Phys. Chem.*, 1971, **75**, 991–1024.
29 A. K. Sakhiya, A. Anand, V. K. Vijay and P. Kaushal, *Energy Nexus*, 2021, **4**, 100026.
30 C.-F. Lin, W.-T. Tseng and M. S. Feng, *J. Appl. Phys.*, 2000, **87**, 2808–2815.
31 G. Socrates, *Infrared and Raman Characteristic Group Frequencies: Tables and Charts*, John Wiley & Sons, 2004.
32 F. R. Mansour, M. A. A. Hamid, A. Gamal and S. H. Elagamy, *J. Food Compos. Anal.*, 2024, **127**, 105972.
33 R. V. Pawar, P. O. Patil, M. Khalid, S. Wahab, M. Taleuzzaman, S. R. Pardeshi and Z. G. Khan, *J. Fluoresc.*, 2025, 1–16.
34 K.-W. Sung, K.-Y. Ko and H.-J. Ahn, *J. Energy Storage*, 2023, **72**, 108797.
35 M. Chaghaghazardi, S. Kashanian, M. Nazari, K. Omidfar, Y. Joseph and P. Rahimi, *Spectrochim. Acta, Part A*, 2023, **293**, 122448.
36 P. Yu, X. Wen, Y.-R. Toh and J. Tang, *J. Phys. Chem. C*, 2012, **116**, 25552–25557.
37 Y. Wang, S. Kalytchuk, Y. Zhang, H. Shi, S. V. Kershaw and A. L. Rogach, . *Phys. Chem. Lett.*, 2014, **5**, 1412–1420.
38 Y. Jiang, Q. Han, C. Jin, J. Zhang and B. Wang, *Mater. Lett.*, 2015, **141**, 366–368.
39 H. Ding, S.-B. Yu, J.-S. Wei and H.-M. Xiong, *ACS Nano*, 2016, **10**, 484–491.
40 X. Huo, H. Shen, R. Liu and J. Shao, *ACS Omega*, 2021, **6**, 26499–26508.
41 V. Manikandan and N. Y. Lee, *Environ. Res.*, 2022, **212**, 113283.
42 M. Fu, F. Ehrat, Y. Wang, K. Z. Milowska, C. Reckmeier, A. L. Rogach, J. K. Stolarczyk, A. S. Urban and J. Feldmann, *Nano Lett.*, 2015, **15**, 6030–6035.
43 K. G. Nguyen, I.-A. Baragau, R. Gromicova, A. Nicolaev, S. A. Thomson, A. Rennie, N. P. Power, M. T. Sajjad and S. Kellici, *Sci. Rep.*, 2022, **12**, 13806.
44 X. Jin, X. Sun, G. Chen, L. Ding, Y. Li, Z. Liu, Z. Wang, W. Pan, C. Hu and J. Wang, *Carbon*, 2015, **81**, 388–395.
45 Z. S. Qian, X. Y. Shan, L. J. Chai, J. R. Chen and H. Feng, *Biosens. Bioelectron.*, 2015, **68**, 225–231.
46 Y. Shin, J. Lee, J. Yang, J. Park, K. Lee, S. Kim, Y. Park and H. Lee, *Small*, 2014, **10**, 866–870.
47 O. Ustun, S. N. Karadag, H. Mazlumoglu, A. Yilmaz and M. Yilmaz, *Coatings*, 2023, **13**, 456.
48 C. A. Zamora-Valencia, M. I. Reyes-Valderrama, L. Escobar-Alarcón, V. Garibay-Febles and V. Rodríguez-Lugo, *Crystals*, 2025, **15**, 206.
49 C. Moldovan, *et al.*, *Pharmaceutics*, 2021, **13**, 1556.
50 K. J. Powell, P. L. Brown, R. H. Byrne, T. Gajda, G. Hefter, S. Sjöberg and H. Wanner, *Pure Appl. Chem.*, 2005, **77**, 739–800.
51 E. Florez, A. D. Zapata-Escobar, F. Ferraro, C. Ibargüen Becerra, Y. Chamorro and A. F. Maldonado, *J. Phys. Chem. A*, 2023, **127**, 8032–8049.
52 W. Duan, J. Wang, L. Chang, L. Zhao, Z. Tian, Z. Huang and W. Huang, *RSC Adv.*, 2018, **8**, 38259–38269.
53 M. Ugrina, T. Čeru, I. Nuić and M. Trgo, *Processes*, 2020, **8**, 1523.
54 J. A. Dean, *Lange's Handbook of Chemistry*, McGraw-Hill Professional, New York, 15th edn, 1999.
55 W. Yao, Y. Hua, Z. Yan, C. Wu, F. Zhou and Y. Liu, *RSC Adv.*, 2021, **11**, 36310–36318.
56 E. Dhandapani, P. Maadeswaran, R. M. Raj, V. Raj, K. Kandiah and N. Duraisamy, *Mater. Sci. Eng., B*, 2023, **287**, 116098.
57 H. Fu, Z. Ji, X. Chen, A. Cheng, S. Liu, P. Gong, G. Li, G. Chen, Z. Sun, X. Zhao, *et al.*, *Anal. Bioanal. Chem.*, 2017, **409**, 2373–2382.
58 J. Hou, J. Li, J. Sun, S. Ai and M. Wang, *RSC Adv.*, 2014, **4**, 37342–37348.
59 A. Kamal, S. Hong and H. Ju, *Biosensors*, 2025, **15**, 99.
60 Y. Yang, T. Zou, Z. Wang, X. Xing, S. Peng, R. Zhao, X. Zhang and Y. Wang, *Nanomaterials*, 2019, **9**, 738.
61 S. Wu, C. Zhou, C. Ma, Y. Yin and C. Sun, *J. Chem.*, 2022, **2022**, 3737646.
62 Z. Zhan, J. Cai, Q. Wang, Y. Su, L. Zhang and Y. Lv, *Luminescence*, 2016, **31**, 626–632.
63 Y. Du and S. Guo, *Nanoscale*, 2016, **8**, 2532–2543.
64 O. A. Aladesuyi and O. S. Oluwafemi, *Inorg. Chem. Commun.*, 2023, **153**, 110843.
65 K. Kasinathan, S. Samayanan, K. Marimuthu and J.-H. Yim, *Appl. Surf. Sci.*, 2022, **601**, 154266.
66 G. L. Long and J. D. Winefordner, *Anal. Chem.*, 1983, **55**, 712A–724A.
67 L. A. Currie, *Anal. Chim. Acta*, 1999, **391**, 105–126.
68 Codex Alimentarius Commission, General Standard for Contaminants and Toxins in Food and Feed (CXS 193-1995), 1995, Updated edition.
69 European Commission, Commission Regulation (EC) No 1881/2006 of 19 December 2006 setting maximum levels for certain contaminants in foodstuff, Official Journal of the European Union, 2006, vol. **L364**, pp. 5–24.
70 U.S. Food and Drug Administration, Fish and Fishery Products Hazards and Controls Guidance, 2020, Chapter on Mercury.
71 D. Gu, S. Shang, Q. Yu and J. Shen, *Appl. Surf. Sci.*, 2016, **390**, 38–42.
72 Y. Hao, R. Li, Y. Liu, X. Zhang, L. Geng and S. Chen, *J. Fluoresc.*, 2023, **33**, 459–469.
73 F. Yan, Z. Bai, F. Zu, Y. Zhang, X. Sun, T. Ma and L. Chen, *Microchim. Acta*, 2019, **186**, 113.
74 X. Zhang, Y. Zhang, Y. Wang, S. Kalytchuk, S. V. Kershaw, Y. Wang, P. Wang, T. Zhang, Y. Zhao, H. Zhang, *et al.*, *ACS Nano*, 2013, **7**, 11234–11241.
75 X. Hu, X. An and L. Li, *Mater. Sci. Eng., C*, 2016, **58**, 730–736.
76 Y. Guo, L. Zhang, F. Cao and Y. Leng, *Sci. Rep.*, 2016, **6**, 35795.
77 H. Liu, H. Xu and H. Li, *J. Fluoresc.*, 2022, **32**, 1089–1098.
78 S. Zhu, Q. Meng, L. Wang, J. Zhang, Y. Song, H. Jin, K. Zhang, H. Sun, H. Wang and B. Yang, *Angew. Chem., Int. Ed.*, 2013, **52**, 3953–3957.